



Monitoring freshwater salinization in analog transport models by time-lapse electrical resistivity tomography

Florian M. Wagner^{a,b,*}, Marcus Möller^a, Cornelia Schmidt-Hattenberger^a, Thomas Kempka^a, Hansruedi Maurer^b

^a Helmholtz Centre Potsdam, GFZ German Research Centre for Geosciences, Telegrafenberg, 14473 Potsdam, Germany

^b ETH Zurich, Institute of Geophysics, Sonneggstrasse 5, 8092 Zurich, Switzerland

ARTICLE INFO

Article history:

Received 25 June 2012

Accepted 16 November 2012

Available online 5 December 2012

Keywords:

Salinization

Brine migration

Sandbox

Electrical resistivity tomography

Numerical flow and transport simulations

ABSTRACT

Deep saline aquifers are target formations both for the geological storage of carbon dioxide as well as for geothermal applications. High pressure gradients, resulting from fluid or gas injection processes, provide a potential driving force for the displacement of native formation waters, implicating a potential salinization of shallow freshwater resources. Geoelectrical monitoring techniques are sensitive to compositional changes of groundwater resources, and hence capable to detect salinization processes at an early stage. In this context, numerical simulations and analog modeling can provide a valuable contribution by identifying probable salinization scenarios, and thereby guiding an optimum sensor network layout within the scope of an early warning system. In this study, coupled numerical flow and transport simulations of a laterally uniform salinization scenario were carried out and used to support a subsequent realization in a laboratory sandbox model. During the experiment, electrical resistivity tomography (ERT) was applied in a practical surface–borehole setup in order to determine the spatio-temporal variations of electrical properties influenced by saltwater intrusion. Inversion results of different electrode configurations were evaluated and compared to numerical simulations. With regard to surface–borehole measurements, good results were obtained using crossed bipoles, while regular bipole measurements were more susceptible to noise. Within the scope of a single-hole tomography, the underlying resistivity distribution was best reproduced using the Wenner configuration, which was substantiated by synthetic modeling.

© 2012 Elsevier B.V. Open access under [CC BY-NC-ND license](https://creativecommons.org/licenses/by-nc-nd/4.0/).

1. Introduction

Geological storage of CO₂ has received considerable attention as a technology to support the transition to low-carbon energy systems, while being consistent with continued fossil fuel use. On a global scale, deep saline aquifers offer the highest storage capacity for CO₂ (IPCC, 2005) and are also target formations for geothermal applications. Synergetic utilization of geothermal energy and CO₂ storage is part of ongoing research (e.g. Pruess and Spycher, 2010; Randolph and Saar, 2011) and may be a sustainable concept to combine renewable and transitional energy technologies.

Several hydrogeological aspects have to be considered, when deep saline aquifers are engineered for storage and production activities. General water challenges of carbon capture and storage operations (e.g. water demand for the capture process) as well as potential impacts on shallow freshwater resources have been reviewed recently by Newmark et al. (2010) and Lemieux (2011). One key concern is

the potential upward migration of native formation fluids through hydraulic conduits driven by induced pressure gradients. Upon intrusion into shallow aquifers, brine can lead to significant freshwater salinization and potentially limit the use of freshwater resources for domestic, agricultural and industrial applications.

High resolution monitoring concepts are sorely needed to identify preferential flow pathways of saline water and thereby allowing countermeasures to be taken in time prior to large-scale groundwater deterioration. Geoelectrical monitoring techniques are particularly suited to detect freshwater salinization, as electrical properties of the medium are directly sensitive to compositional changes in the pore-filling fluid. As part of an integrated monitoring concept, the electrical resistivity tomography (ERT) can provide useful information on the near-surface region and the vicinity of (electrodes-equipped) boreholes. A number of case studies have demonstrated the value of ERT to detect freshwater salinization (e.g. Bauer et al., 2006; de Franco et al., 2009; Maurer et al., 2009; Nguyen et al., 2009), whereby most of the work is related to seawater intrusion in coastal areas. Although important principles can be derived from these studies, the application to CO₂ storage related salinization is not straightforward and requires further (site-specific) research, as salinities, flow rates and spatial extent of the salinization scenario may differ considerably.

* Corresponding author at: Helmholtz Centre Potsdam, GFZ German Research Centre for Geosciences, Telegrafenberg, 14473 Potsdam, Germany. Tel.: +49 331 288 28739; fax: +49 331 288 1502.

E-mail address: florian.wagner@gfz-potsdam.de (F.M. Wagner).

Since geoelectrical field data from prospective storage sites is usually scarce, numerical simulations and analog laboratory experiments play an important role during the planning phase of reliable monitoring systems in advance to their field-scale implementation. ERT has been successfully applied in analog transport modeling studies to image and characterize the movement of conductive saline tracers through unconfined sediments (Slater et al., 2000, 2002) and undisturbed soils (Binley et al., 1996; Koestel et al., 2008; Olsen et al., 1999). In this study, we experimentally simulate pressure-driven upward migration of a synthetic brine through an initially freshwater-saturated porous medium in a laboratory sandbox model. In doing so, we evaluate the monitoring performance of frequently used electrode configurations carrying out a miniaturized ERT survey in a practical surface–borehole setup. The workflow includes numerical flow and transport simulations of the selected salinization scenario, which serve as the basis for a synthetic ERT study and are additionally used to support the experimental procedure and to validate the monitoring results.

2. Experimental and numerical transport modeling

2.1. Experimental design and procedure

A schematic cross-section of the experimental setup is shown in Fig. 1. The cylindrical sandbox consists of acrylic glass and has a height of 640 mm and an inner diameter of 634 mm. Thus, it comprises a volume of approximately 200 l, which corresponds to about 300 kg of dry sand (assuming a density of $1,600 \text{ kg/m}^3$). A total of 100 mounting-holes at the walls allow flexible drainage and sensor placement. For this experiment, connections for recharge and discharge were drilled at four opposite positions close to the bottom and the top of the tank, respectively (Fig. 1). Saltwater injection into the tank was realized by employing a peristaltic pump connected to a suction pipe. The cylinder was positioned on a customized laboratory desk, which incorporates a load cell facilitating in-situ porosity determinations.

In this study, laterally uniform brine migration through a homogeneous medium is investigated. A gravel filter layer was incorporated at the bottom of the model to allow for a widespread and non-localized upward migration of the injected saline solution. After filling the gravel to a height of 9 cm and addition of water, an in-situ porosity of 32% was determined and adopted in the numerical model (Table 1). With the aim of preventing the considerably smaller sand grains to slip into the large pore volume of the underlying gravel, a textile filter was positioned in between both layers. Prior to sand

emplacement, a vertical electrode array was positioned and fixed in the center of the sandbox. Sand filling was performed incrementally, meaning that a certain amount of water was added to the tank and sand was emplaced subsequently. During this procedure, the amount of inserted sand grains was chosen carefully in order to avoid air entrapment. Very fine sequences developed, which were reduced by mixing the sand during sedimentation. Controlled percussions at the sides of the sandbox led to near-wall consolidation counteracting wall effects. No further efforts were made towards compaction of the medium.

As a consequence of the wet packing method, the medium was prepared to be fully saturated with freshwater at the beginning of the experiment. Subsequently, a highly saline solution with a NaCl concentration of 200 g/l solution, as to be expected in deep saline aquifers relevant for geological CO_2 storage (Michael et al., 2010), was injected via four opposite inlets vertically centered with respect to the gravel layer. The injection rate of 10 ml/min was kept constant over a period of six days providing a steady pressure gradient for the upward movement of the denser saltwater. A fiber optic refractive index sensor (FISO Technologies, Québec, Canada) placed at the outflow of the sandbox provided salinity measurements of the effluent every ten minutes. Thereby, salt arrival at the top of the sandbox was captured to validate the prediction from numerical flow and transport simulation.

2.2. Material characterization

The homogeneous medium was prepared with a well-sorted Fontainebleau sand, which is frequently used in laboratory sandbox studies (e.g. Allègre et al., 2010; Bordes et al., 2006). To adequately parameterize the numerical flow and transport model, hydraulic properties of the material were determined in advance. A constant-head permeameter yielded a permeability of 23 Darcy. This value is in good agreement with calculations on the basis of empirical formulas (Fair and Hatch, 1933; Harleman and Melhorn, 1963), reflecting good sorting of the sand. Bulk porosities were determined gravimetrically in containers of different volumes and in the sandbox setup applied. Porosity calculations are based on the total volume, the sand mass and the amount of water added to ensure full saturation. Laboratory measurements revealed a porosity of 37% for the medium sand opposed to 44% obtained in the sandbox model. This large value may reflect the loose packing of the material immediately after emplacement. Similar contrasts were observed in the experiments of Slater et al. (2002). For numerical simulations, a bulk porosity of 40% was assumed.

2.3. Numerical model setup

Numerical flow and transport simulations of the selected saltwater migration scenario on the laboratory scale were performed using TOUGH2 (Pruess, 1991; Pruess et al., 1999). TOUGH2 is a general-purpose fluid and heat flow simulator applied for multi-dimensional, multi-component and multi-phase flow and transport processes in porous and fractured media. In this study, the ECO2N module (Pruess, 2005) was employed, which comprises the thermodynamics and thermophysical properties for mixtures of water, NaCl and CO_2 . Although influences of temperature and CO_2 were not considered in the simulations, the module provides all relevant equations of state for the calculation of isothermal salt transport at room temperature.

The conceptual model consists of a cylindrical boundary according to the sandbox dimensions. Cells outside of the boundary act as an impermeable boundary condition (Neumann type). Discharge is realized by a top layer with an increased permeability and an infinite volume, which has its base at the vertical position of the upper drains of the sandbox. The large volume of the top boundary condition cells ensures that flow into the top layer has a negligible effect on pressure.

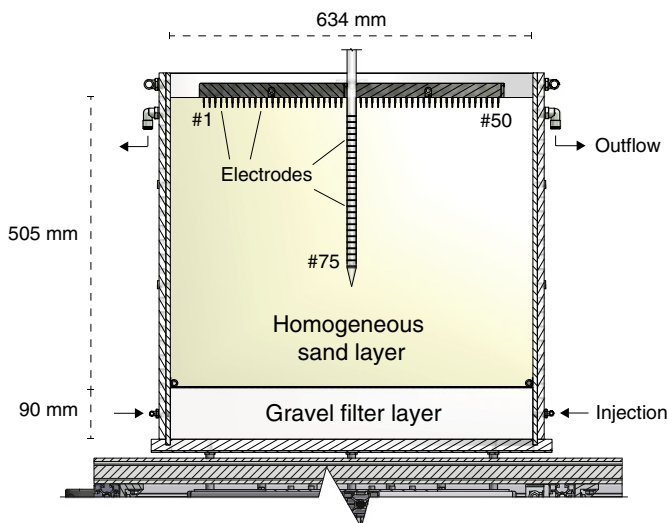


Fig. 1. Cross-sectional view of the laboratory sandbox model showing the electrode layout of the two-dimensional image plane.

Table 1
Input parameters of the numerical flow and transport model.

	Parameter	Symbol	Value	Unit	Substantiation
General	Temperature	T	20	°C	Tap water temperature
	Grid spacing	$\Delta x, \Delta y, \Delta z$	15	mm	Grid convergence test
	Diffusion coefficient	D_m	0	m ² /s	Numerical simulations
	NaCl concentration	C_{NaCl}	200	g/l solution	Defined
	Injection rate	Q	10	ml/min	Defined
Sand	Porosity	ϕ	0.4	–	Laboratory and in-situ determination
	Permeability	k	$2.29 \cdot 10^{-1}$	m ²	Laboratory experiments
Gravel	Porosity	ϕ	0.32	–	In-situ determination
	Permeability	k	$1.0 \cdot 10^{-9}$	m ²	Assumed

Consequently, these boundary cells maintain their initial (atmospheric) pressure and represent a *Dirichlet* boundary condition. The conceptual model also incorporates the gravel filter layer and is shown in Fig. 2. In correspondence to the experimental procedure, injection was realized via four opposite cells, vertically centered with respect to the gravel layer.

According to a sensitivity analysis undertaken, molecular diffusion does not play a role for the upward movement of saltwater on the investigated timescale and was therefore neglected. Consequently, the transport problem is treated as being purely advective. Simulations were carried out by means of coupled flow and transport. Hence, the gravity effect of the injected saline solution on the resulting flow field is taken into account. The model domain was spatially discretized using regular blocks. To ensure numerical stability without unnecessarily increasing computational demands, stepwise grid refinement and subsequent evaluation of the simulation results were carried out in order to find a reasonable degree of fineness. Based on this grid convergence test, the model was discretized in 13,960 cells (Fig. 2). Further grid refinement did not lead to notable changes in the simulated distribution of NaCl in both spatial and temporal terms. Parameterization of the conceptual model is summarized in Table 1. The combination of an analog transport model and corresponding numerical simulations provides a well-defined saltwater intrusion scenario for the validation of geoelectrical monitoring as discussed hereafter.

3. ERT monitoring of saltwater intrusion

3.1. Data acquisition

During the saltwater intrusion experiment, resistivity measurements were carried out in a two-dimensional image plane comprising one vertical and two horizontal electrode strings. The three electrode strings were arranged in a 'T-formation', facilitating surface, single-hole and surface–borehole measurements. Each string consists of 25

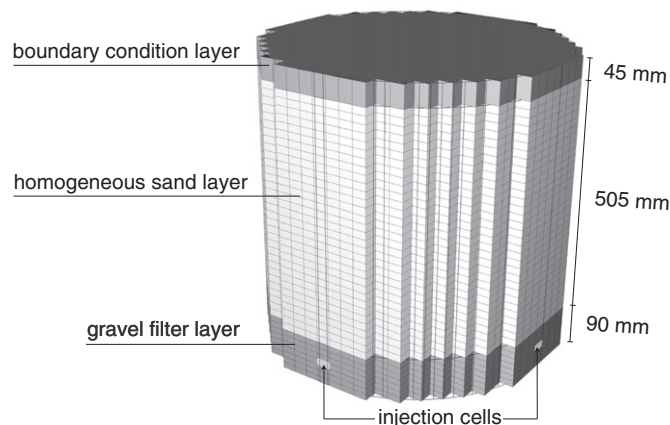


Fig. 2. Conceptual model incorporating a gravel filter and a top boundary condition layer.

electrodes spaced by 1 cm, resulting in a setup with a total number of 75 electrodes, as illustrated in Fig. 1. The 50 surface electrodes are gold-plated copper alloy pins of 18 mm length and 2 mm diameter. Vertically positioned electrodes are ring-shaped and have a height of 1 mm and a diameter of 16 mm. Measurements were performed nearly continuous over a period of one week. Employed electrode configurations include regular bipole, crossed bipole, Wenner and Schlumberger measurements and are illustrated in Fig. 3. Note that borehole configurations are shown horizontally, although they were employed on the vertical array. The arrow indicates the direction of progress and encompasses the moving electrodes. Separation a (i.e. unit spacing of electrodes) defines the distance of active current and potential electrodes and was varied in the measurement protocol. Abbreviations and acquisitional parameters of the configurations are listed in Table 2. The total acquisition time was approximately 4 h and 20 min. Including proper buffers between the individual configurations, the measuring schedule was repeated every 5 h.

3.2. Data error analysis

Tomographic inversions of geoelectrical data sets are strongly affected by the reliability of error estimates. Overestimation decreases resolution and results in exaggerated smoothing, while underestimation can lead to severe artifacts (LaBrecque et al., 1996). In ERT studies, error assessment is typically based on either repeatability or reciprocity checks, while the latter (i.e. interchange of current and potential electrodes) can detect errors that may be left unrecognized in the former case (e.g. LaBrecque et al., 1996; Slater et al., 2000). However, reciprocal measurements significantly stress acquisition time (potentially by a factor of two), which is in conflict to a high temporal resolution for capturing dynamic flow processes. To avoid temporal smearing caused by long acquisition times and in the interest of incorporating all configurations within a reasonable time window, reciprocal measurements were omitted. Therefore, error estimation in this study is based on the coefficient of variation inferred from stacked potential measurements, which give an indication of the measurement repeatability. For the inversion, a constant Gaussian error model is assumed, in which the estimated absolute error ($|e|$) increases with the magnitude of the measured resistance ($|R|$) according to:

$$|e| = \varepsilon_m + \varepsilon_r |R|. \quad (1)$$

Here, ε_m denotes a minimum error component and ε_r describes the variation of the absolute error as a function of the measured resistance. The corresponding plot is given in Fig. 4. Obvious outliers (red circles) were sorted out by means of pre-defined bounds based on empirical knowledge, that is, measurements with an absolute resistance larger than 1700 Ω and coefficients of variation above 5%. Following the approach of Slater et al. (2000), the remaining reliable data was enveloped by a straight line, where the intercept and the slope define the error model parameters $\varepsilon_m = 0.01$ and $\varepsilon_r = 0.039$ in Eq. (1). This relation represents the maximum error to be expected and was applied to calculate the diagonal terms of the data weighting

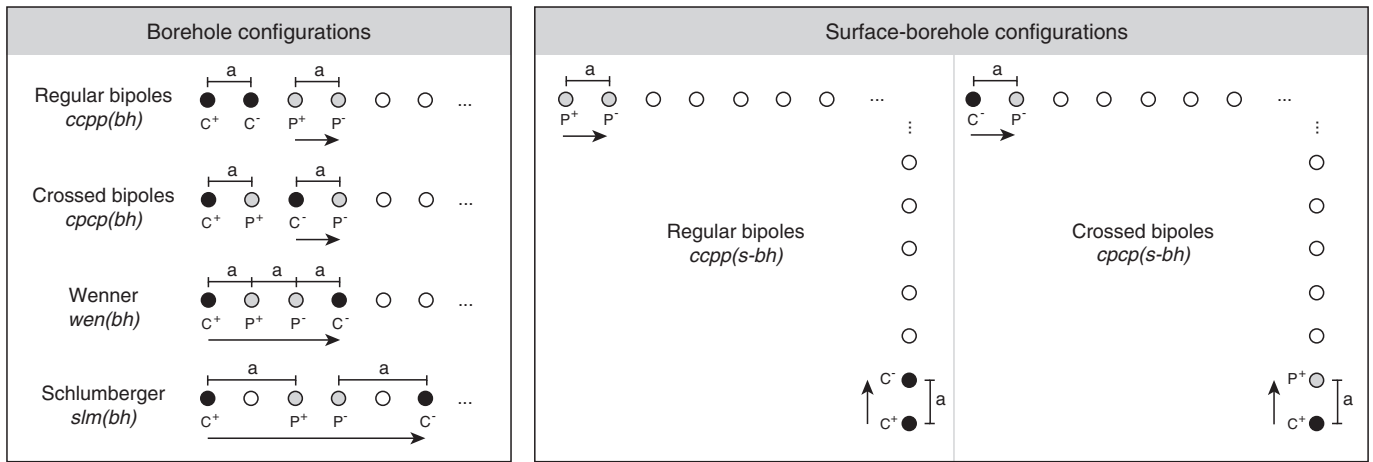


Fig. 3. Employed electrode configurations.

matrix \mathbf{W}_d (Eq. (2)). This error estimation was necessary to stabilize the inversion procedure, as the use of the individual data errors led to convergence problems.

Data filtering according to the defined bounds led to a data reduction by about 4%, whereby the majority of disregarded measurements was recorded using the regular bipole configuration (zoomed inlay in Fig. 4). This reflects its inherent susceptibility to noise, especially for small bipole spacings and large distances between both bipole pairs. Data filtering did not reduce the data sets obtained by the borehole configurations (except for regular bipole measurements), reflecting good electrical coupling compared to the horizontal array. This is most likely the result of occasional evaporation. The outlets were located 2 cm beneath the surface of the medium to prevent flooding of the electrode casings (Fig. 1). Due to this distance and relatively small capillary forces of the unconfined sand, the upper part was not fully saturated at all times of the experiment. This upper unsaturated part (in a way representing a vadose zone) is the reason for several exceptionally high resistance measurements, as one unsaturated pore may already have a notable influence on the measurement, considering the small size of the electrodes. However, randomly applied coupling tests showed no indication of poor electrode contact. In a final step, short distance measurements across both horizontal electrode strings (electrodes 24 to 27 in Fig. 1) were neglected, as they were considerably influenced by the electrically insulating PVC casing of the vertical array.

3.3. Tomographic inversion procedure

In this study, three-dimensional geoelectrical modeling and inversion was performed with the software package *R3t* (Binley, 2011), which proved to be well suited for closed laboratory setups in previous studies (e.g. Koestel et al., 2008; Olsen et al., 1999). To accurately account for the sandbox geometry, a three-dimensional cylindrical finite-element representation was generated using the software package *gms* (Geuzaine and Remacle, 2009). One half of the parameter mesh is shown in Fig. 6. The free surface as well as the electrically

insulating bottom and circumferential edges of the sandbox were honored by applying *Neumann* boundary conditions (current density perpendicular to the boundary is forced to zero) to all sides of the finite element mesh.

Three-dimensional current flow and the resulting potential distribution were solved numerically for a cylindrical mesh composed of 141,400 triangular prism elements. To limit the degrees of freedom of the geoelectrical inverse problem and the associated computational effort, a resistivity parameter was assigned to clusters of four laterally adjacent elements as illustrated in Fig. 6. With a total number of 35,360 parameters the inverse problem is still highly ill-posed as encountered in field situations. For the sake of comparison, all subsequent models were computed based on one forward and one inversion mesh.

An estimate of the model parameters \mathbf{m} (electrical resistivities) is obtained by minimizing the following regularized objective function (Binley and Kemna, 2005):

$$\Psi(\mathbf{m}) = \|\mathbf{W}_d[\mathbf{d} - \mathbf{f}(\mathbf{m})]\|^2 + \alpha \|\mathbf{W}_m(\mathbf{m} - \mathbf{m}_{\text{ref}})\|^2. \quad (2)$$

The first term penalizes the data misfit between measured data \mathbf{d} and forward modeled resistances $\mathbf{f}(\mathbf{m})$, where \mathbf{W}_d is a data weighting matrix based on the reciprocals of the data error. To account for the wide range of encountered resistivities, log-transformed values have been assigned to \mathbf{d} and \mathbf{m} . The second term in Eq. (2) imposes a regularization constraint on the parameter search. The model weighting (or roughness) matrix \mathbf{W}_m , together with the difference term enclosed by the brackets, accounts for the spatial extent and nature of smoothing between adjacent parameter cells and the deviation from a certain reference model \mathbf{m}_{ref} . Although the main purpose of this term is to stabilize the inversion, it can be used to incorporate a priori information (Daily et al., 2005). In this case, a homogeneous resistivity distribution of 12 Ωm is assigned to the reference model \mathbf{m}_{ref} in Eq. (2). This value corresponds to the estimated resistivity of freshwater-saturated sand based on Archie's Law and is used for the inversion of all timesteps. Various tests showed that the choice of the initial model does not

Table 2
Acquisitional parameters of employed electrode configurations.

Type	No. of electrodes	Configuration	Abbreviation	Electrode separations (a)	No. of measurements
Borehole	25	Regular bipoles	ccpp (bh)	1, 2	353
		Crossed bipoles	cpcp (bh)	1, 2	353
		Wenner	wen (bh)	1–8	92
		Schlumberger	slm (bh)	2–11	110
Surface-borehole	75	Regular bipoles	ccpp (s-bh)	1, 2	2280
		Crossed bipoles	cpcp (s-bh)	1, 2	2280

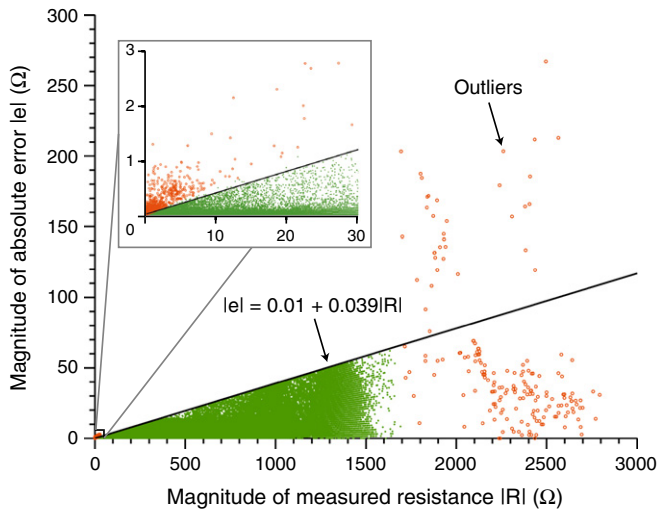


Fig. 4. Magnitude of absolute error plotted against magnitude of measured resistance for 258,947 individual measurements. Outliers are marked in red. The enveloping line defines the error model parameters in Eq. (1). The zoomed inlay emphasizes the small and error-prone regular bipole measurements.

affect the inverse solutions of the time-lapse data sets in both qualitative and quantitative terms.

As evident from Eq. (2), the regularization parameter α balances the influence of data and model misfit. Since resistivity contrasts were assumed to be predominately vertical, more smoothing in the horizontal direction was allowed in this study ($\alpha_h/\alpha_v = 2$). The iterative scheme used to minimize Eq. (2) is based on a Gauss–Newton approach and discussed more extensively in Kemna (2000) and Binley and Kemna (2005). The iteration process was stopped, when the chi-squared data misfit reached a value of 5. Smaller tolerance limits resulted in severe imaging artifacts.

3.4. Relating NaCl concentration to electrical resistivity

In order to correlate inverted resistivity profiles to fluid salinities, and thereby allowing for a quantitative comparison of ERT monitoring and numerical simulation results, a relationship between sodium chloride concentration and fluid conductivity was established. In addition, such a relationship enables synthetic ERT measurements to be

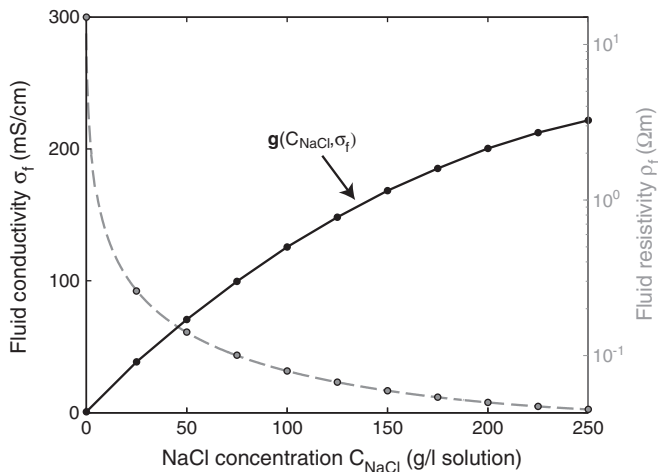


Fig. 5. Electrical fluid properties as a function of NaCl concentration. The polynomial g was fitted to fluid conductivity values. Fluid resistivity, the reciprocal, is plotted in gray (dashed line) on a semi-logarithmic scale.

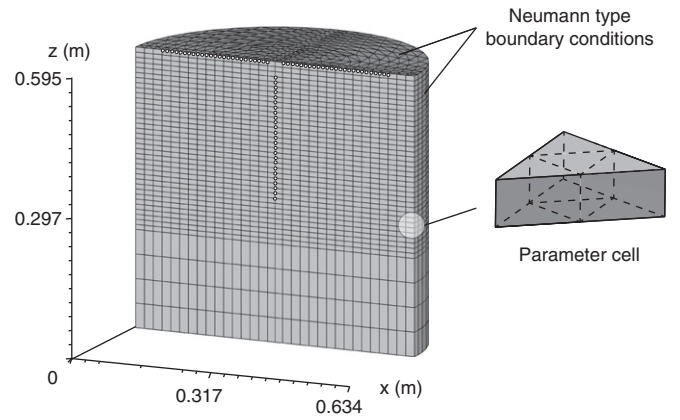


Fig. 6. One half of the parameter mesh resulting from a split through the image plane. The zoomed section illustrates how a model parameter is composed of four laterally adjacent forward modeling cells.

made for simulated saltwater migration scenarios. Conductivity measurements were performed on twelve fluid samples with increasing concentrations up to 275 g/l solution. These measurements were repeated at three different fluid temperatures of 17, 21 and 22 °C, while deviations were fairly small (± 0.44 mS/cm). Since tap water temperature variation within this range was inevitable, the mean value was considered in this study. In most studies, the dependency of fluid conductivity to salt concentration is described by linear regression (e.g. Nguyen et al., 2009; Oswald, 1998; Singha and Gorelick, 2005). Such an approximation is reasonable for specific salinity intervals, where electrolytic conduction is directly proportional to the amount of free dissolved ions. Another necessity for this approximation may arise in the case of data scarcity. For example, Nguyen et al. (2009) only considered the salinities of freshwater and seawater available from well samples and linearly interpolate between both.

In this study, salinities ranging from tap water salinity (treated as 0 g/l solution) to a NaCl concentration of 200 g/l solution were encountered. At these high concentrations, the large amount of dissolved ions hinders the mobility of each individual charged particle, leading to a reduction in conductivity increase at higher concentrations as discernible in Fig. 5. This behavior was described by a second order polynomial function $g(C_{NaCl}, \sigma_f)$, which fits the measured values reasonably well (coefficient of determination $R^2 = 0.99$). Under the assumption that electrolytic conduction exerts a major control on the bulk geoelectrical response and that the medium was fully saturated at all times during the experiment, simulated NaCl concentration was converted to bulk electrical resistivity using a simple form of Archie's Law (Archie, 1942):

$$\rho = g(C_{NaCl})^{-1} \cdot a\phi^{-m}. \quad (3)$$

In analogy, ERT-derived NaCl concentration estimates were obtained by applying the relationship in an inverse mode. Here C_{NaCl} [g/l solution] is the NaCl concentration and ρ [Ωm] is the bulk electrical resistivity of the medium. This proportionality is scaled by the formation factor ($F = a\phi^{-m}$), accounting for the presence of a non-conducting matrix. It represents an empirical factor correlated to the total porosity ($\phi = 0.4$), a cementation factor (m) and a proportionality constant usually equal to one for unconsolidated sediments (Schön, 1996). The cementation factor accounts for the connectivity of the pore space and is known to vary between 1.3 and 2.2 for sandstones depending on the degree of consolidation (Doveton, 1986; Guyod, 1944). Since a pure, unconsolidated sand was used in this study and emplaced without any efforts towards compaction, a value of $m = 1.3$ was used, yielding a formation factor of $F = 3.29$.

4. Results

4.1. Comparison of numerical and experimental transport models

Saltwater arrival in the effluent was observed at the fourth day. Fig. 7 compares the arrival curve obtained from the salinity sensor at the outflow of the tank to the prediction from numerical flow and transport modeling. Note that local minima and variations in the measured curve result from dilution effects in the outflow container (and from emptying it). A notable fit is obtained by numerical modeling without any history matching applied. However, the simulated curve predicts the first increase in salinity to be slightly earlier. This small mismatch can be most likely attributed to inaccuracies of the model parameterization due to the lack of detailed porosity and permeability data. Although care was attributed to a uniform sand emplacement, formation of heterogeneities was unavoidable. As a result, uneven discharge at the four outflow hoses was observed during the experiment. Nevertheless, the good agreement between the two curves proves that numerical simulation was successful in supporting the experiment in both qualitative and quantitative terms. This substantiates the use of the flow and transport model as the basis for synthetic ERT modeling.

4.2. Tomographic inversions of synthetic ERT data

To assess the ability of the individual configurations in reconstructing the expected vertical resistivity gradient, a synthetic ERT study was performed on the basis of the numerical flow and transport model. For this purpose, the vertical resistivity gradient was derived from the simulated saltwater distribution after three days of injection using Eq. (3). Subsequently, the geoelectrical forward problem was solved for all configurations and 5% Gaussian distributed noise was added to the data. Inversion of the synthetic data sets was carried out similarly to inversion of the measured data as described in Section 3. Note that for the sake of visualization, all subsequent inversion results focus on the main image plane resulting from a slice through the three-dimensional volume as depicted in Fig. 6.

4.2.1. Borehole configurations

Fig. 8a–d shows the reconstructed tomograms of all four borehole configurations. The underlying resistivity distribution used to solve the forward problem is shown in Fig. 8e. All four borehole

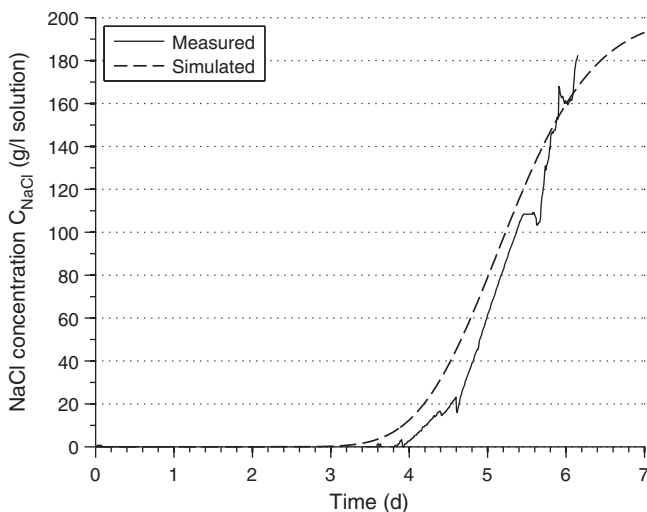


Fig. 7. Saltwater arrival curves obtained from the fiber optic sensor at the outflow of the tank in comparison to numerical model prediction.

configurations are able to reconstruct the resistivity gradient in the vicinity of the vertical array. The color saturation is linearly scaled to the upper half of the normalized cumulative sensitivity. The tomograms reveal that configurations with small potential electrode spacings, i.e. regular bipole (Fig. 8a) and Schlumberger (Fig. 8b) measurements, seem to notably underestimate the maximum resistivity, while crossed bipole (Fig. 8c) and Wenner (Fig. 8d) measurements perform well on the whole depth interval. As a measure of goodness, Fig. 8f compares the Frobenius norm of the difference between the estimated model parameters (\mathbf{m}) and the underlying resistivity distribution used for forward calculations (\mathbf{m}^{true}) of all four configurations according to:

$$\|\mathbf{m} - \mathbf{m}^{\text{true}}\|_F = \sqrt{\sum_{i=1}^m \sum_{j=1}^n |m_{ij} - m_{ij}^{\text{true}}|^2}. \quad (4)$$

The indices i and j refer to the position of the model cell within the two-dimensional image plane (Fig. 6), i.e. only the elements occupying the plane constituted by the acquisition geometry are considered for the calculation of the difference norm. Notwithstanding the smallest number of individual data points (Table 2), the Wenner configuration best reproduces the underlying resistivity distribution reflected in the lowest magnitude of the corresponding difference norm.

4.2.2. Surface–borehole configurations

Fig. 9 compares the tomographic inversions of regular and crossed bipole data, synthetically derived from the resistivity distribution shown in Fig. 8e. Resistivity information recovered by regular bipole measurements is focused around the centered part of the horizontal array and the upper part of the vertical array (Fig. 9a). In contrast, crossed bipole measurements exhibit lateral continuity in the upper part of the medium and a better reconstruction of the low resistive region, although sensitivity at greater depth is not enhanced compared to borehole measurements (Fig. 8).

4.3. Tomographic inversions of experimental ERT data

4.3.1. Borehole configurations

Inverse modeling results of all four borehole configurations are plotted in Fig. 10. The underlying data sets were recorded after three days (± 2 h) of saltwater injection. To enhance time-varying features, the tomograms show relative changes in electrical resistivity throughout the image plane according to:

$$\Delta\rho = \frac{\rho - \rho_0}{\rho_0} \cdot 100\%, \quad (5)$$

where ρ is the (individually) inverted resistivity at a particular point in time (post-injection) and ρ_0 is the corresponding reference resistivity measured under freshwater-saturated conditions (pre-injection).

All four borehole configurations reveal a significant resistivity change at a depth of approximately 0.4 m. As a result of the relatively small spacing between both potential electrodes, sensitivity of the regular bipole configuration (Fig. 10a) is limited in x-direction compared to the inversion results of Schlumberger (Fig. 10b), crossed bipole (Fig. 10c) and Wenner (Fig. 10d) measurements. Salient are the artifacts produced by the crossed bipole configuration in close proximity to the electrodes. This may be attributed to the relatively unusual arrangement, i.e. the overlapping of current and potential bipoles, resulting in large positive and negative sensitivity values close to the electrodes. In combination with the presence of the electrically insulating PVC casing, this characteristic is a likely cause of the artifacts present in the tomogram in Fig. 10c. In contrast, the Wenner configuration (Fig. 10d), where both potential electrodes are enclosed by the current source and the current sink, is less affected by noise

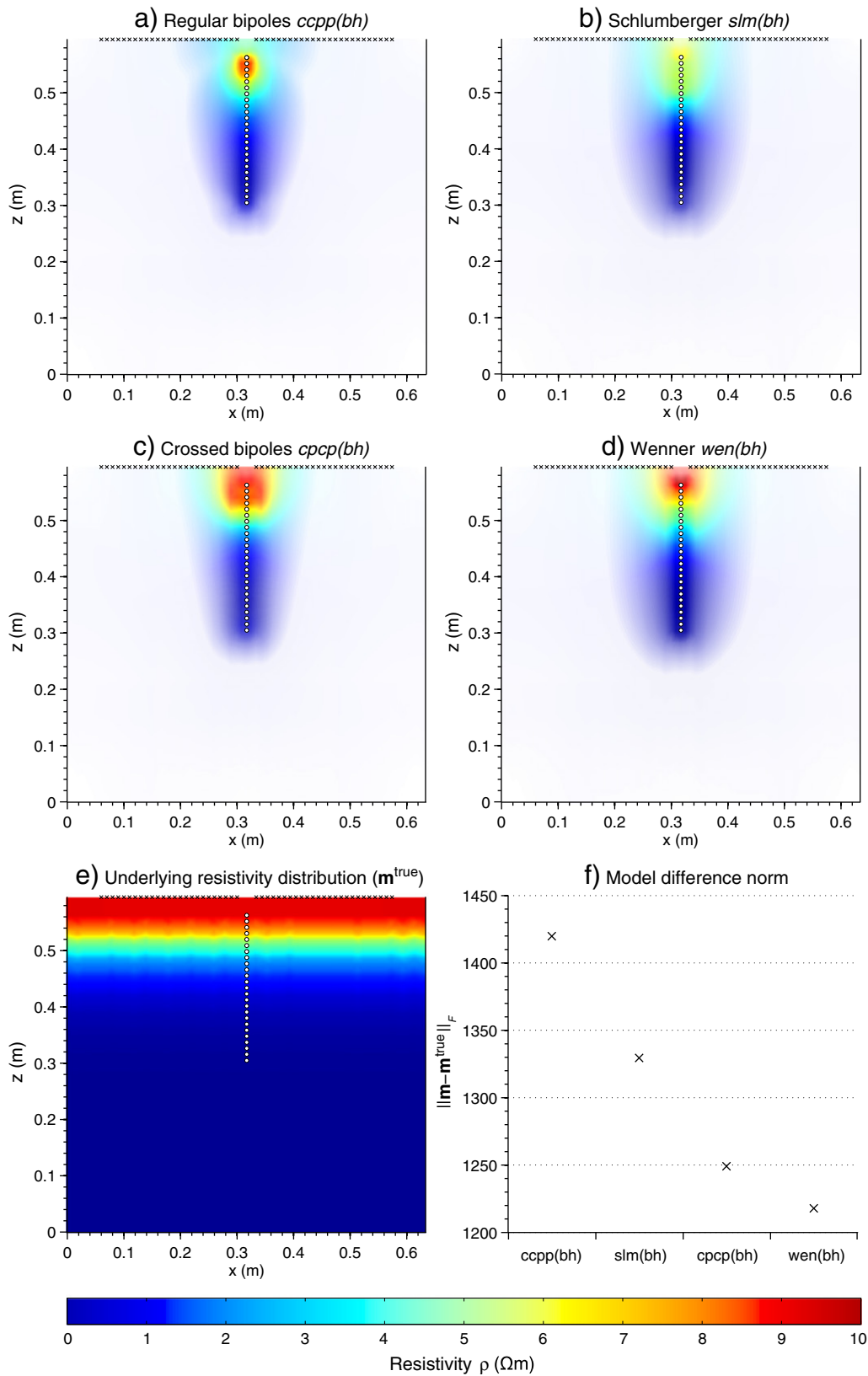


Fig. 8. Tomographic inversions of synthetic borehole data obtained by (a) regular bipole, (b) Schlumberger, (c) crossed bipole and (d) Wenner configurations. Color saturation is adjusted according to the logarithmic cumulative sensitivity. (e) Underlying resistivity distribution. (f) Frobenius norm of the difference between the underlying resistivity model used for forward calculations and the corresponding inversion result of all four borehole configurations.

and comparable in terms of lateral sensitivity. In fact, the Wenner array yields the best result of all four borehole configurations, while having the smallest number of individual measurements.

The good performance of the configuration is likely a result of the high signal strength and the fact that the separation between all active electrodes was varied throughout the measuring sequence. To

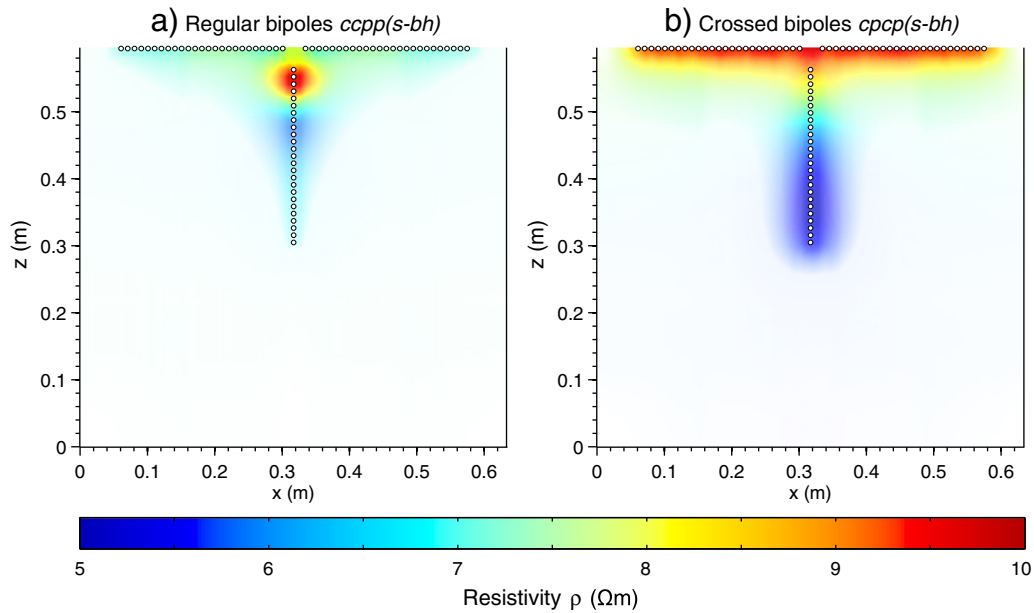


Fig. 9. Tomographic inversions of synthetic data obtained by (a) regular and (b) crossed bipole configurations in a surface–borehole setup. The degree of color saturation is scaled by the logarithm of the respective cumulative sensitivity.

emphasize the ability of the Wenner array to map temporal resistivity changes, a time-lapse sequence is shown in Fig. 11. The first indication of a resistivity decline is observed at the third day (Fig. 11a). Subsequent movement of the saltwater front can be well inferred from the strong resistivity contrast, which is shifted upwards over time. Similar time-lapse results could be obtained using the other borehole configurations, while obtained resistivity information is constrained to the vicinity of the vertical array in all tomograms.

4.3.2. Surface–borehole configurations

Due to the unfavorable geometric arrangement, i.e. the small bipole spacings with respect to the relatively large distance of current and potential electrodes in a surface–borehole setup, the signal-to-noise ratio of regular bipole measurements was vanishingly low. This has also been verified during data error analysis (Section 3.2). On an average, the measured voltages using the regular bipole configuration were approximately 0.2 mV, which is two orders of magnitude smaller compared to crossed bipole measurements. To further illustrate the noisy character of regular compared to crossed bipole measurements, the relative change of the mean absolute resistance is plotted in Fig. 12 for both configurations.

The mean absolute resistance of crossed bipole measurements is not subject to notable changes until it smoothly decreases starting at the third day of saltwater injection. A comparable behavior was observed for the borehole configurations. On the contrary, regular bipole measurements show a rather random behavior and exhibit mean absolute resistance changes of up to 170%. Note that changes in the mean measured response are considered here, while individual changes of resistance measurements reached exorbitant values. As a consequence thereof, no resistivity distribution was found during tomographic inversion, which fits the regular bipole data sets, whereas inversions of crossed bipole data converged readily. Fig. 13 shows relative changes in electrical resistivity obtained from crossed bipole measurements for selected time steps. Note that a different scale is used in the interest of visualization, since crossed bipole measurements generally measured higher resistances and smaller relative changes due to the large spacing of both potential electrodes.

The incorporation of the horizontal array clearly reveals resistivity variations in the upper part of the sand layer, where the medium was

only partially saturated during the experiment (Fig. 13). Although saltwater outflow already occurred at the point in time at which the data set was recorded ($t=4$ days), the first decline in resistivity in the vicinity of the vertical array is detected approximately at $z=0.5$ m, which is in agreement with the corresponding inverse models of all four borehole configurations. This means that either the configurations were not capable of detecting the upward movement of small concentrations in the vicinity of the vertical array, or more likely, that this upward movement was not laterally uniform as predicted by the numerical simulations for a homogeneous medium. Saltwater migration outside of the sensitive area of the array, especially along the tank wall, may be the cause of this mismatch. Additional information on lateral inhomogeneities can be obtained from ERT-derived arrival curves as discussed hereafter.

4.4. ERT-derived NaCl arrival curves

Fig. 14a shows three discrete probe locations throughout the image plane in proximity to the vertical (A and B) and the horizontal array (C). Fig. 14a,b and c provide the corresponding arrival curves. The simulated curve is extracted from numerical flow and transport simulation results at the corresponding locations. Since points B and C are located close to the vertical position of the outlets, the salinity curve measured at the outflow of the tank is plotted in addition as a reference.

Given the simplicity of the petrophysical relation as well as the errors inherent in geoelectrical data acquisition and tomographic inversion, the ERT-derived arrival curves are in significantly good agreement to measured and simulated results. A good accordance can be observed particularly in the vicinity of the vertical array, where high sensitivity is given and full saturation of the medium ensured good electrical coupling. The more distinct temporal disagreement in Fig. 14c reflects the observed unevenness of discharge at the four outflow hoses, where preferential flow to one outlet may have left some parts in the near-surface region completely unaffected by saltwater intrusion.

As a consequence of the loss of resolution, resistivity further away from the arrays was not recovered accurately enough to allow for quantitative estimates of NaCl concentrations. Nevertheless,

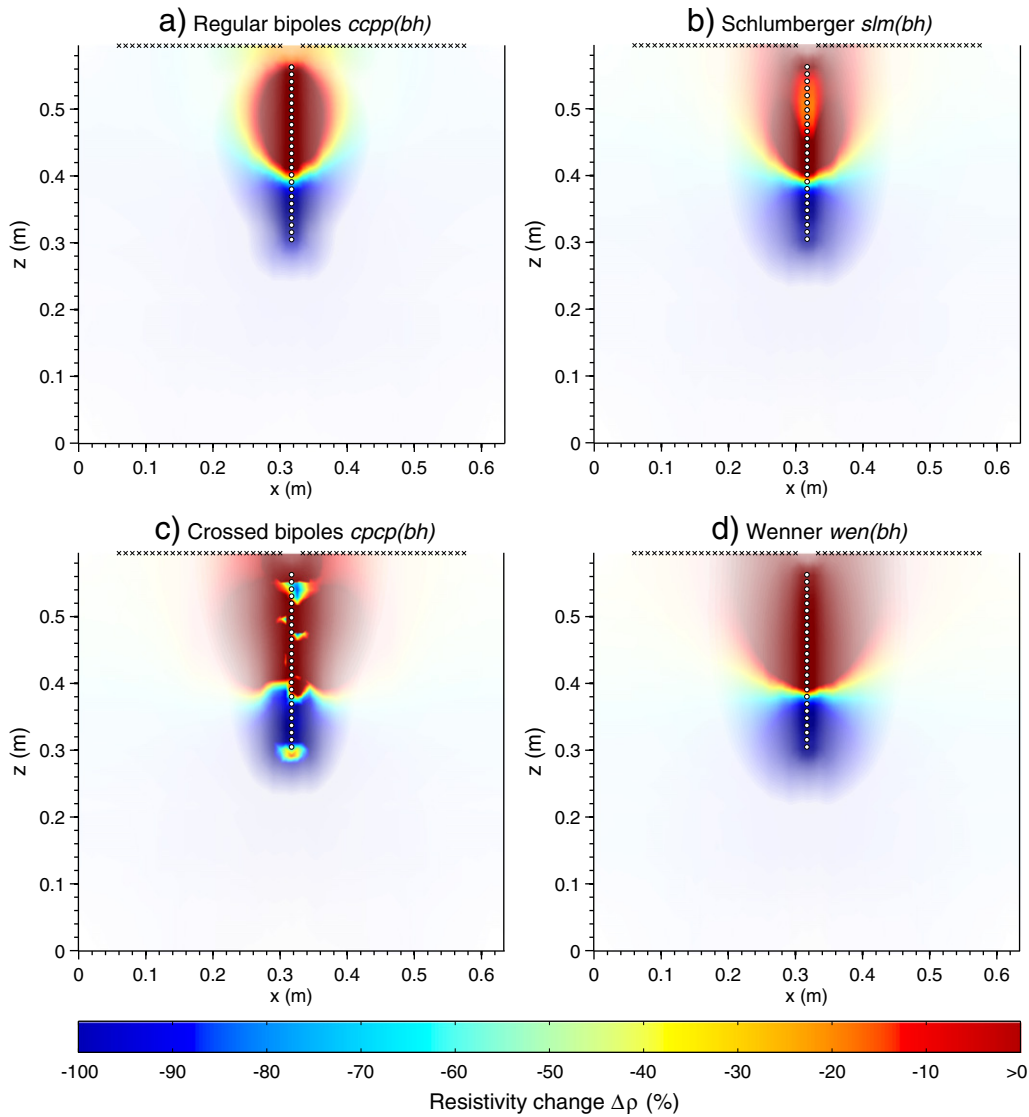


Fig. 10. Tomographic inversions of all four borehole configurations showing relative changes in electrical resistivity after three days of saltwater injection. Color saturation is scaled by the logarithm of the cumulative sensitivity.

Fig. 14 shows that geoelectrical monitoring was able to detect and quantitatively describe the saltwater arrival, and moreover, that this arrival was well predicted by numerical flow and transport simulations.

5. Conclusions

The value of time-lapse ERT to detect spatial and temporal variations of saltwater intrusion was demonstrated using a laboratory sandbox

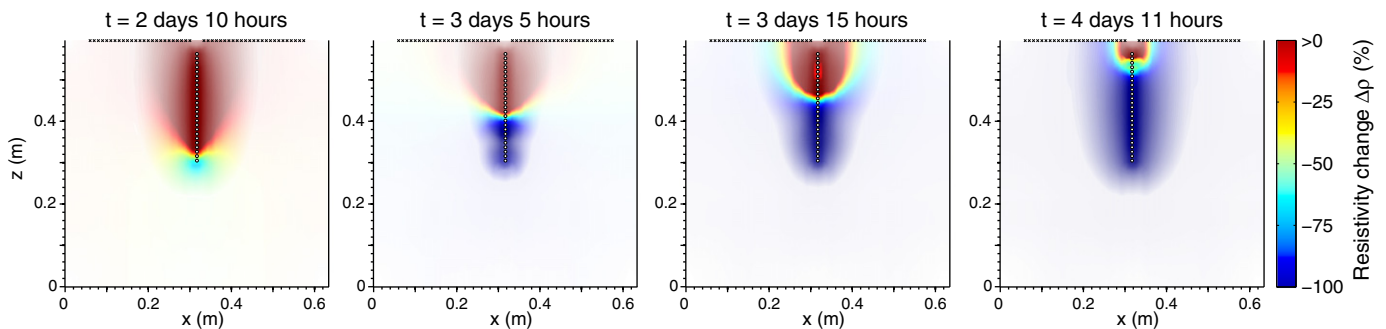


Fig. 11. Relative changes in electrical resistivity obtained from Wenner borehole measurements for selected time steps. Color saturation corresponds to the logarithmic cumulative sensitivity.

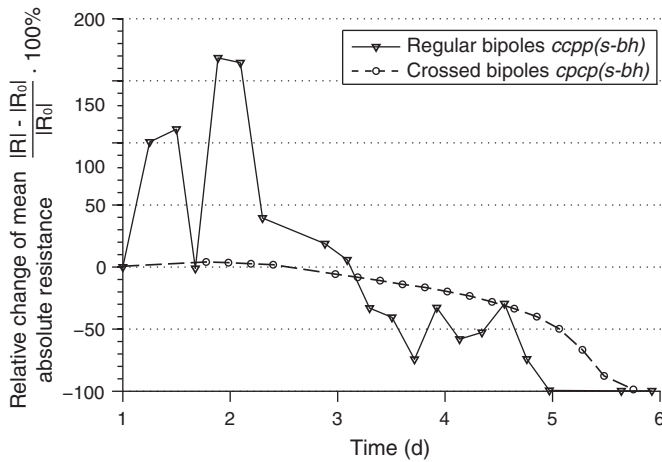


Fig. 12. Time-dependent relative change of the mean absolute resistance with respect to freshwater-saturated conditions of regular and crossed bipole measurements in a surface–borehole setup.

model. From this study, some relevant conclusions can be drawn with regard to field-scale early warning systems. This study showed that for a surface–borehole setup using a single vertical array and a laterally uniform upward movement of saltwater, the crossed bipole configuration yielded the by far best results, while regular bipole measurements exhibited considerable low signal-to-noise ratios for small bipole spacings and large separations of both bipole pairs. With regard to the small spacing of the electrodes relative to their size, it should be noted that a finite discretization of the electrodes using a complete electrode model (CEM) can lead to more accurate solutions (Rücker and Günther, 2011). In general, the variation of both current and potential electrode spacings has shown to be decisive for the depth of penetration and obtained absolute resistivity values.

All borehole configurations provided a good reconstruction of the resistivity contrast, underlining the usefulness of single-hole ERT to detect brine migration in the vicinity of boreholes. As evidenced by synthetic modeling, the Wenner configuration outperformed the remaining configurations, while having the smallest number of individual measurements. In this study, the performance of borehole and surface–borehole configurations was evaluated separately. Obviously, it is worthwhile to combine both measurement types in field applications to benefit from high resolution in the vicinity of the vertical array and in the near-surface region. In this case, it may be necessary to adapt the inversion scheme with appropriate weighting factors to account for symmetric artifacts associated with single-hole measurements (Tsourlos et al., 2011).

The experiment demonstrated that vertically positioned electrodes were inevitable for depth-related resistivity information, and therefore

crucial for an early detection of saltwater intrusion. Although the incorporation of horizontal electrodes revealed near surface heterogeneities of saltwater migration, sensitivity at greater depth was not notably enhanced compared to borehole configurations. This demonstrates that the imaging capability of surface–borehole measurements using a single well is inherently limited. Perri et al. (2012) come to a similar conclusion by comparing cross-hole and surface ERT monitoring results of a field tracer test. In accordance with injection and observation wells at a potential CO₂ storage site, the incorporation of multiple vertical arrays is advisable. Since this may facilitate cross-hole measurements, surface electrodes can then be additionally employed in a semi-permanent or mobile manner as required.

Further research is required to formulate relevant guidelines for an optimum monitoring concept to detect freshwater salinization within the scope of field-scale early warning systems. Choosing suitable (standard and non-standard) electrode configurations to optimally exploit subsurface information is generally of great interest in resistivity surveying and part of ongoing research (e.g. Blome et al., 2011; Stummer et al., 2004; Wilkinson et al., 2012). Experimental design for freshwater salinization early warning systems remains particularly challenging, given the wide variety of probable saltwater intrusion scenarios (e.g. wide-spread or localized, varying flow rates). In this regard, numerical flow simulations can provide valuable information on the more likely scenarios. Within the scope of an early warning system, it may be worthwhile to identify configurations that are most sensitive to the spatial (e.g. Furman et al., 2007; Henning et al., 2008) and temporal development of the predicted saltwater migration scenarios.

Although an optimum sensor layout is subject to a variety of site-specific factors, controlled laboratory experiments allow to identify favorable configurations depending on a given intrusion scenario. In future work, we will carry out additional sandbox studies with different sensor layouts and electrode configurations as well as different salinization scenarios in order to identify those setups that are applicable to a wide variety of saltwater intrusion patterns. Furthermore, the effect of varying salinity on the geoelectrical response is studied insufficiently. The steep decline of fluid resistivity at small NaCl concentrations, followed by minor changes at concentrations above 100 g/l solution (Fig. 5), gives rise to the question, whether geoelectrical techniques are generally capable of detecting resistivity variations above a certain salinity threshold. Moreover, varying injection rates could elucidate the effect of temporal smearing in the obtained tomograms. Laboratory-scale transport models are also well suited to improve the quantification of solute transport processes by means of geoelectrical monitoring. Although, aside from the fact that a quantitative description may not be the main priority for early warning systems, transferring derived principles to the field scale is challenging, since the relation between salinity and conduction is much more complex and certainly not constant throughout the image plane as postulated in this study.

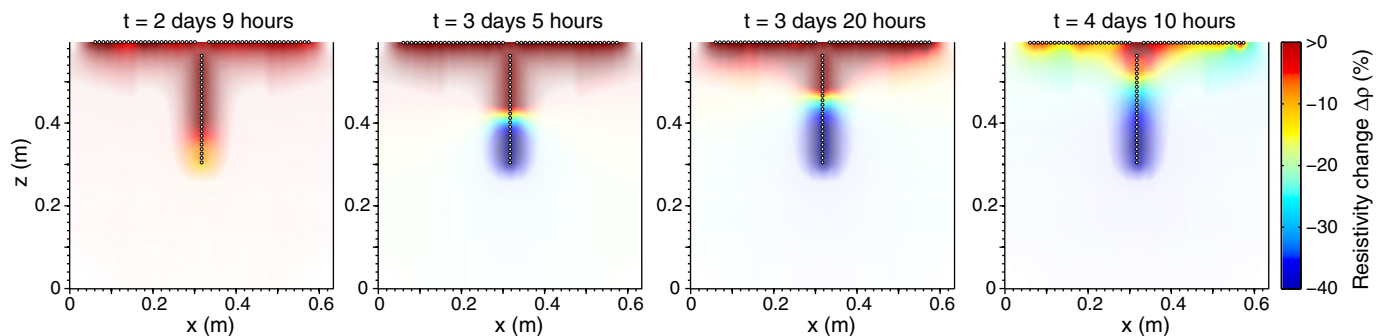


Fig. 13. Relative changes in electrical resistivity obtained from crossed bipole surface–borehole measurements for selected timesteps. The logarithmic cumulative sensitivity determines the degree of color saturation.

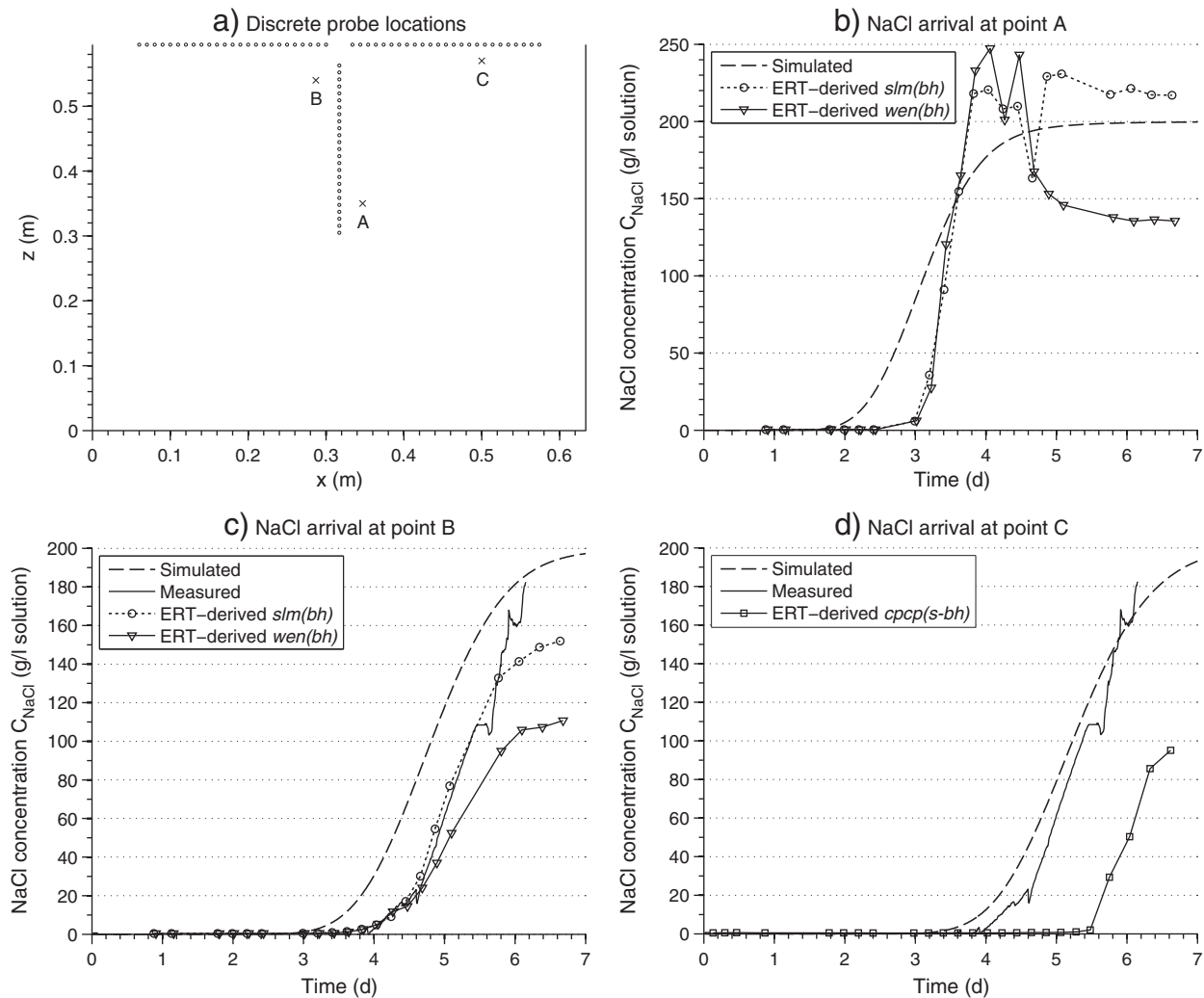


Fig. 14. Comparison of NaCl arrival curves obtained from numerical flow and transport simulations, an optical sensor mounted at the outflow of the sandbox and petrophysical conversion of ERT monitoring results. Three discrete probe locations throughout the image plane are marked in panel (a). Panels (b), (c) and (d) show the corresponding arrival curves.

Ultimately, the usefulness for field-scale applications should be the main priority of analog transport modeling studies.

Acknowledgments

This is publication No. GEOTECH-2000 of the GEOTECHNOLOGIEN program financially supported by the German Federal Ministry of Education and Research (BMBF) within the frame of the R&D project *brine* (grant 03G0758A). We thank Andrew Binley for the instructions with regard to the use of his inversion code and gratefully acknowledge the support of several helpers during the experimental work. The insightful comments of Andreas Weller and one anonymous reviewer considerably improved the clarity of the manuscript.

References

- Allègre, V., Jouniaux, L., Lehmann, F., Sailhac, S., 2010. Streaming potential dependence on water-content in Fontainebleau sand. *Geophysical Journal International* 182, 1248–1266.
- Archie, G.E., 1942. The electrical resistivity log as an aid in determining some reservoir characteristics. *Transactions of the American Institute of Mining, Metallurgical and Petroleum Engineers (Trans AIME)* 146, 54–62.
- Bauer, P., Supper, R., Zimmermann, S., Kinzelbach, W., 2006. Geoelectrical imaging of groundwater salinization in the Okavango Delta, Botswana. *Journal of Applied Geophysics* 60, 126–141.
- Binley, A., 2011. R3t Version 1.5a. http://www.es.lancs.ac.uk/people/amb/Freeware/R3t/R3t_readme.pdf.
- Binley, A., Kemna, A., 2005. Dc resistivity and induced polarization methods. In: Rubin, Y., Hubbard, S. (Eds.), *Hydrogeophysics*.
- Binley, A., Shaw, B., Henry-Poulter, S., 1996. Flow pathways in porous media: electrical resistance tomography and dye staining image verification. *Measurement Science and Technology* 7, 384–390.
- Blome, M., Maurer, H., Greenhalgh, S.A., 2011. Geoelectric experimental design — efficient acquisition and exploitation of complete pole–bipole data sets. *Geophysics* 76, F15–F26.
- Bordes, C., Jouniaux, L., Dietrich, M., Pozzi, J.P., Garambois, S., 2006. First laboratory measurements of seismic-magnetic conversions in fluid-filled Fontainebleau sand. *Geophysical Research Letters* 33, L01302.
- Daily, W., Ramirez, A., Binley, A., LaBrecque, D.J., 2005. Electrical resistance tomography — theory and practice. *Society of Exploration Geophysicists (SEG)* 525–547 (Ch. 17).
- de Franco, R., Biella, G., Tosi, L., Teatini, P., Lozej, A., Chiozotto, B., Giada, M., Rizzetto, F., Claude, C., Mayer, A., Bassan, V., Gasparetto-Stori, G., 2009. Monitoring saltwater intrusion by time lapse electrical resistivity tomography: the Chioggia test site (Venice Lagoon, Italy). *Journal of Applied Geophysics* 69, 117–130.
- Doveton, J.H., 1986. *Log Analysis of Subsurface Geology*. John Wiley and Sons, Inc.
- Fair, G.M., Hatch, L.P., 1933. Fundamental factors governing the streamline flow of water through sand. *Journal of American Water Works Association* 25, 1551–1565.
- Furman, A., Ferré, T.P.A., Heath, G.L., 2007. Spatial focusing of geoelectrical resistivity surveys considering geologic and hydrologic layering. *Geophysics* 72, F65–F73.
- Geuzaine, C., Remacle, J.F., 2009. Gmsh: a three-dimensional finite element mesh generator with built-in pre- and post-processing facilities. *International Journal for Numerical Methods in Engineering* 79, 1309–1331.
- Guyod, H., 1944. *Electrical Well Logging*. Halliburton Oil Well Cementing Company.
- Harleman, D.R.F., Melhorn, P.F., 1963. Dispersion–permeability correlation in porous media. *American Society of Civil Engineers* 89, 67–85.
- Henning, T., Weller, A., Möller, M., 2008. Object orientated focussing of geoelectrical multielectrode measurements. *Journal of Applied Geophysics* 65, 57–64.

- IPCC, 2005. IPCC Special Report on Carbon Dioxide Capture and Storage: Prepared by Working Group III of the Intergovernmental Panel on Climate Change. Technical Report. Cambridge University Press.
- Kemna, A., 2000. Tomographic inversion of complex resistivity – theory and application, Ph.D. thesis, Ruhr-Universität Bochum.
- Koestel, J., Kemna, A., Javaux, M., Binley, A., Vereecken, H., 2008. Quantitative imaging of solute transport in an unsaturated and undisturbed soil monolith with 3-D ERT and TDR. *Water Resources Research* 44, W12411.
- LaBrecque, D.J., Miletto, M., Daily, W., Ramirez, A., Owen, E., 1996. The effects of noise on Occam's inversion of resistivity tomography data. *Geophysics* 61, 538–548.
- Lemieux, J.-M., 2011. Review: the potential impact of underground geological storage of carbon dioxide in deep saline aquifers on shallow groundwater resources. *Hydrogeology Journal* 19, 757–778.
- Maurer, H., Friedel, S., Jaeggi, D., 2009. Characterization of a coastal aquifer using seismic and geoelectric borehole methods. *Near Surface Geophysics* 7, 353–366.
- Michael, K., Golab, A., Shulakova, V., Ennis-King, J., Allinson, G., Sharma, S., Aiken, T., 2010. Geological storage of CO₂ in saline aquifers – a review of the experience from existing storage operations. *International Journal of Greenhouse Gas Control* 2, 659–667.
- Newmark, R.L., Friedmann, S.J., Carroll, S.A., 2010. Water challenges for geologic carbon capture and sequestration. *Environmental Management* 45, 651–661.
- Nguyen, F., Kemna, A., Antonsson, A., Engesgaard, P., Kuras, O., Ogilvy, R., Gisbert, J., Jorrete, S., Puidlo-Bosch, A., 2009. Characterization of seawater intrusion using 2D electrical imaging. *Near Surface Geophysics* 7, 377–390.
- Olsen, P.A., Binley, A., Henry-Poulter, S., Tych, W., 1999. Characterizing solute transport in undisturbed soil cores using electrical and X-ray tomographic methods. *Hydrological Processes* 13, 211–221.
- Oswald, S., 1998. Variable density flow in porous media: three-dimensional experiments and modelling, Ph.D. thesis, Swiss Federal Institute of Technology Zurich.
- Perri, M.T., Cassiani, G., Gervasio, I., Deiana, R., Binley, A., 2012. A saline tracer test monitored via both surface and cross-borehole electrical resistivity tomography: comparison of time-lapse results. *Journal of Applied Geophysics* 79, 6–16.
- Pruess, K., 1991. Tough2 – A General-Purpose Numerical Simulator for Multiphase Fluid and Heat Flow. Report LBNL-29400 Lawrence Berkeley National Laboratory, Berkeley, CA, USA. (URL <http://www.osti.gov/geochemical/servlets/purl/5212064-3iINC8/5212064.pdf>).
- Pruess, K., 2005. Eco2n: A TOUGH2 Fluid Property Module for Mixtures of Water, NaCl, and CO₂. Report LBNL-57952. Lawrence Berkeley National Laboratory, Berkeley, CA, USA. (URL http://esd.lbl.gov/tough2/eco2n_man.pdf).
- Pruess, K., Spycher, N., 2010. Enhanced geothermal systems (egs) with CO₂ as heat transmission fluid – a scheme for combining recovery of renewable energy with geologic storage of CO₂. LBNL-1949E. Paper Presented at the World Geothermal Congress 2010. International Geothermal Association (IGA), Bali, Indonesia (April 25–29, 2010).
- Pruess, K., Oldenburg, C.M., Moridis, G., 1999. Tough2 User's Guide. Report LBNL-43134. Lawrence Berkeley National Laboratory, Berkeley, CA, USA. (URL http://esd.lbl.gov/TOUGH2/LBNL_43134.pdf).
- Randolph, J.B., Saar, M.O., 2011. Combining geothermal energy capture with geologic carbon dioxide sequestration. *Geophysical Research Letters* 38, L10401.
- Rücker, C., Günther, T., 2011. The simulation of finite ERT electrodes using the complete electrode model. *Geophysics* 76, F227–F238.
- Schön, J.H., 1996. Physical Properties of Rocks: Fundamentals and Principles of Petrophysics. Pergamon Press.
- Singha, K., Gorelick, S.M., 2005. Saline tracer visualized with three-dimensional electrical resistivity tomography: field-scale spatial moment analysis. *Water Resources Research* 41, W05023.
- Slater, L., Binley, A., Daily, W., Johnson, R., 2000. Cross-hole electrical imaging of a controlled saline tracer injection. *Journal of Applied Geophysics* 44, 85–102.
- Slater, L., Binley, A., Versteed, R., Cassiani, G., Birken, R., Sandberg, S., 2002. A 3D ERT study of solute transport in a large experimental tank. *Journal of Applied Geophysics* 49, 211–229.
- Stummer, P., Maurer, H., Green, A.G., 2004. Experimental design: electrical resistivity data sets that provide optimum subsurface information. *Geophysics* 69, 120–139.
- Tsoulos, P., Ogilvy, R., Papazachos, C., Meldrum, P., 2011. Measurement and inversion schemes for single borehole-to-surface electrical resistivity tomography surveys. *Journal of Geophysics and Engineering* 8, 487–497.
- Wilkinson, P.B., Loke, M.H., Meldrum, P.I., Chambers, J.E., Kuras, O., Gunn, D.A., Ogilvy, R., 2012. Practical aspects of applied optimized survey design for electrical resistivity tomography. *Geophysical Journal International* 189, 428–440.